

Precursor Wave Emission Enhanced by Weibel Instability in Relativistic Shocks

MASANORI IWAMOTO,¹ TAKANOBU AMANO,¹ MASAHIRO HOSHINO,¹ AND YOSUKE MATSUMOTO²

¹*Department of Earth and Planetary Science, University of Tokyo, 7-3-1 Hongo, Bunkyo-ku, Tokyo 113-0033, Japan*

²*Department of Physics, Chiba University, 1-33 Yayoi, Inage-ku, Chiba, Chiba 263-8522, Japan*

ABSTRACT

We investigated the precursor wave emission efficiency in magnetized purely perpendicular relativistic shocks in pair plasmas. We extended our previous study to include the dependence of upstream magnetic field orientations. We performed two-dimensional particle-in-cell simulations and focused on two magnetic field orientations: the magnetic field to be in the simulation plane (i.e., in-plane configuration) and perpendicular to the simulation plane (i.e., out-of-plane configuration). Our simulations in the in-plane configuration demonstrated that not only extraordinary but also ordinary mode waves are excited. We quantified the emission efficiency as a function of the magnetization parameter σ_e and found that the large-amplitude precursor waves are emitted for a wide range of σ_e . We found that especially at low σ_e , the magnetic field generated by Weibel instability amplifies the ordinary mode wave power. The amplitude is large enough to perturb the upstream plasma, and transverse density filaments are generated as in the case of the out-of-plane configuration investigated in the previous study. We confirmed that our previous conclusion holds regardless of upstream magnetic field orientations with respect to the two-dimensional simulation plane. We discuss the precursor wave emission in three dimensions and the feasibility of wakefield acceleration in relativistic shocks based on our results.

Keywords: acceleration of particles — cosmic rays — plasmas — shock waves

1. INTRODUCTION

Observations of active galactic nuclei (AGNs) and gamma ray bursts (GRBs) usually show broad nonthermal spectra (e.g., Kaneko et al. 2006; Abdo et al. 2010), which are believed to originate from synchrotron radiation and inverse Compton scattering of relativistic electrons. Since the relativistic outflow from the central compact object is the common feature in AGNs and GRBs (e.g., Gehrels et al. 2009; Lister et al. 2016), relativistic shocks can be formed upon interaction between the jets and the interstellar medium. The relativistic shocks are assumed to play an important role for generating such nonthermal electrons.

Previous one-dimensional (1D) particle-in-cell (PIC) simulations showed that synchrotron maser instability (SMI) is the significant dissipation mechanism for relativistic magnetized shocks (e.g., Langdon et al. 1988; Gallant et al. 1992; Hoshino et al. 1992; Amato & Arons 2006). The SMI is driven by particles reflected off the

shock-compressed magnetic field in the shock-transition region and emits electromagnetic waves of extraordinary mode (X-mode) both upstream and downstream (Hoshino & Arons 1991). Since the electromagnetic precursor waves have a non-negligible fraction of the upstream kinetic energy, the upstream flow is significantly perturbed by the precursor wave (Lyubarsky 2006). Hoshino (2008) demonstrated that the wave power is strong enough to induce wakefield in the upstream and that nonthermal electrons are generated by wakefield acceleration (WFA; Tajima & Dawson 1979; Chen et al. 2002) in 1D relativistic shocks propagating in magnetized ion–electron plasmas.

In multidimensional systems, it is well known that Weibel instability (WI; Weibel 1959; Fried 1959) develops in the transition region of weakly magnetized shocks. The WI is widely studied in laser plasma as well as astrophysics (e.g., D’Angelo et al. 2015; Huntington et al. 2015, 2017; Park et al. 2015). Previous PIC simulation studies in multiple dimensions demonstrated that the WI grows into substantial amplitude in the shock-transition region at low magnetization $\sigma_e = \omega_{ce}^2/\omega_{pe}^2 \lesssim 10^{-2}$ (e.g., Spitkovsky 2005; Sironi et al. 2013). Here, ω_{ce} is the relativistic electron cyclotron frequency and

ω_{pe} is the proper electron plasma frequency. The effective temperature anisotropy induced by reflected particles in the shock-transition region provides the free energy source for the development of the WI (e.g., Kato 2007; Chang et al. 2008). The linear theory including relativistic effects showed that the maximum growth rate of the WI is on the order of ω_{pe} (see, e.g., Yang et al. 1993; Achterberg et al. 2007; Schaefer-Rolffs & Tautz 2008), whereas that of the SMI is on the order of ω_{ce} (Hoshino & Arons 1991). Since both instabilities are excited from the same free energy source in the same region and ω_{pe} is much greater than ω_{ce} for $\sigma_e \ll 1$, it was believed that the WI dominates over the SMI and the precursor wave emission could be shut off in multi-dimensional shocks.

Recently, by using two-dimensional (2D) PIC simulations, we have shown that the SMI can coexist with the WI and that the precursor wave emission continues to persist even in the Weibel-dominated regime (Iwamoto et al. 2017). We also showed that the wave power is sufficient enough to induce wakefield for a wide range of magnetization parameter σ_e . Based on the results, we suggested that external shocks in the relativistic jets from GRBs may be important sites for the production of ultra-high-energy cosmic rays via WFA.

However, in the previous work, we focused only on perpendicular shock with the upstream ambient magnetic field perpendicular to the simulation plane (i.e., out-of-plane configuration). One may also choose the upstream ambient magnetic field to be in the simulation plane (i.e., in-plane configuration), which may in general change the shock dissipation physics because the degree of freedom in this case becomes three rather than two in the out-of-plane configuration (e.g., Amano & Hoshino 2009). In fact, Sironi et al. (2013) reported that the particle acceleration efficiency in 2D perpendicular shocks depends on the orientation of the pre-shock magnetic field. Therefore, in this study, we consider the in-plane configuration and investigate the physics of magnetized perpendicular shocks, especially the electromagnetic wave emission by the SMI. We quantify the precursor wave emission efficiency and discuss the effects of the magnetic field configuration on the WFA combining this study with our previous results.

This paper is organized as follows. First, Section 2 describes our simulation setup. In Section 3, we show the global structure of relativistic magnetized shocks for relatively high and low magnetization, respectively. In Section 4, the properties of precursor waves are analyzed. In Section 5, we discuss the wave excitation mechanism and the feasibility of the WFA in relativistic magnetized shocks. Finally, Section 6 summarizes this study.

2. SIMULATION SETUP

We carried out simulations of 2D perpendicular shocks in electron-positron plasmas using an electromagnetic PIC code (Matsumoto et al. 2013, 2015). The basic configuration of our simulations is almost identical to our previous simulation (Iwamoto et al. 2017) and schematically illustrated in Figure 1. We changed only the direction of the upstream ambient magnetic field B_1 from the out-of-plane direction (z direction in our coordinate system) to the in-plane direction (y direction).

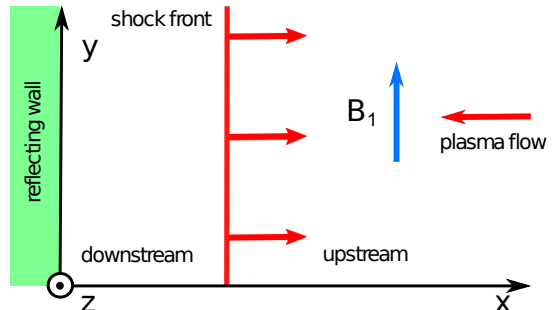


Figure 1. Coordinate system and the orientation of the upstream ambient magnetic field in the present simulation (cf. Iwamoto et al. 2017).

Our simulation domain is in the x - y plane with periodic boundary conditions in the y direction and the number of grids in each direction is $N_x \times N_y = 20,000 \times 1,680$. A cold pair stream is continuously injected along $-x$ direction with a bulk Lorentz factor $\gamma_1 = 40$ from the right-hand boundary and elastically reflected at the left-hand boundary. The shock wave is excited by the interaction between the returning particles and the incoming plasma flow, and propagates toward $+x$ direction. The number of particles per cell in the upstream is $N_1 \Delta x^2 = 64$ for both electrons and positrons, where Δx is the grid size. The grid size is fixed to $\Delta x/(c/\omega_{pe}) = 1/40$ throughout in this study, where c is the speed of light and the ω_{pe} is the proper electron plasma frequency. The proper electron plasma frequency is defined as follows:

$$\omega_{pe} = \sqrt{\frac{4\pi N_1 e^2}{\gamma_1 m_e}}. \quad (1)$$

The number of particles per cell and the grid size are motivated by the numerical convergence study of 1D simulations (see Iwamoto et al. 2017, Appendix A). The time step is set to be $\omega_{pe} \Delta t = 1/40$ in order to minimize the effect of the numerical Cherenkov instability (Ikeya & Matsumoto 2015). For more details, please refer our previous paper (Iwamoto et al. 2017).

As in our previous study, we investigated the dependence of the precursor wave emission on the magnetization parameter σ_e :

$$\sigma_e = \frac{B_1^2}{4\pi\gamma_1 N_1 m_e c^2} = \frac{\omega_{ce}^2}{\omega_{pe}^2}, \quad (2)$$

where ω_{ce} is the relativistic electron cyclotron frequency:

$$\omega_{ce} = \frac{eB_1}{\gamma_1 m_e c}. \quad (3)$$

More specifically, we discuss the results obtained from the following eight runs: $\sigma_e = 1, 3 \times 10^{-1}, 1 \times 10^{-1}, 3 \times 10^{-2}, 1 \times 10^{-2}, 3 \times 10^{-3}, 1 \times 10^{-3}$ and 3×10^{-4} .

3. GLOBAL SHOCK STRUCTURE

3.1. High- σ_e Case

First, we discuss the overview of the global shock structure for relatively high σ_e . Figure 2 is the global shock structure at $\omega_{pe}t = 500$ for $\sigma_e = 3 \times 10^{-1}$. The electron number density N_e , the electron number density averaged along the y axis $\langle N_e \rangle$, the x component of the magnetic field B_x , 1D cut along $y = 21c/\omega_{pe}$ for B_x , the in-plane magnetic field B_y , 1D cut along $y = 21c/\omega_{pe}$ for B_y , the out-of-plane magnetic field B_z , 1D cut along $y/(c/\omega_{pe}) = 21$ for B_z and the electron phase-space density $x-u_{xe}$, $x-u_{ye}$ and $x-u_{ze}$ integrated over the y direction are shown from top to bottom. All quantities are normalized by the corresponding upstream values. Note that our 2D simulations track all three components of the particle velocity and electromagnetic field. A well-developed shock structure is formed at this time, and the shock front is clearly seen at $x/(c/\omega_{pe}) \sim 235$.

At the shock front, fluctuations in B_x are generated. We think the magnetic field fluctuations may be attributed to instabilities excited in the shock-transition region. One of the possible instabilities for this case is the Alfvén-ion-cyclotron instability, which is an electromagnetic instability on the Alfvén mode branch driven by a temperature anisotropy (e.g., Winske & Quest 1988). We perform linear analysis for a relativistic pair plasma with a cold ring distribution and indeed find a similar instability. This instability may be the cause of fluctuations in B_x and the magnetic field energy is eventually amplified up to 10%–20% of the upstream kinetic energy. Although fluctuations in B_z at the shock front may also be generated by the instability, the fluctuations start decreasing in time after $\omega_{pe}t \sim 140$ and are not clearly seen at this time.

The wave magnetic fields δB_y are visible in the upstream region. The electromagnetic waves are continuously emitted from the shock front and persist with large amplitude. Remember that the upstream ambient

magnetic field is in the y direction. The wave magnetic field is polarized in the y direction and parallel to the ambient magnetic field, which is the signature of the X-mode wave (see Section 4.1). This result is consistent with both the linear theory (Hoshino & Arons 1991) and the previous 2D simulation (Iwamoto et al. 2017). The oblique propagation of these X-mode waves may be responsible for the x component of the fluctuating magnetic field δB_x in the upstream region. Since δB_x is very small compared to δB_y , we mainly consider δB_y in our analysis. We think that the waves in the region $x/(c/\omega_{pe}) \gtrsim 460$ are contaminated by the initial and boundary conditions. Therefore, we excluded this region from our analysis presented below.

The wave magnetic fields δB_z are identified in the upstream region. They also appear to be electromagnetic precursor waves emitted from the shock front. The wave magnetic field is polarized in the z direction, and thus the wave mode is the ordinary mode (O-mode; see Section 4.1). This is unexpected because the linear theory of the SMI showed that the growth rate of the O-mode is finite at oblique propagation but much smaller than that of the X-mode (see, e.g., Wu & Lee 1979; Lee et al. 1980; Melrose et al. 1982, 1984). The amplitude of the O-mode wave is smaller than that of the X-mode wave but non-negligible. The tip of the O-mode wave is behind that of the X-mode wave. This delay should result from the difference of the generation time since both have group velocities almost equal to the speed of light. The X-mode waves are generated by the SMI soon after the shock formation in the initial phase of the simulation. In contrast, the generation of the O-mode waves seems to become effective after $\omega_{pe}t \sim 80$, which is estimated from the time evolution of the wave magnetic field δB_z . We discuss how the O-mode waves are excited in Section 5.1 for details.

As in the case of our previous simulation, transverse density filaments are formed in the upstream region. This again indicates that the precursor waves remain large amplitude and coherent in 2D systems.

3.2. Low- σ_e Case

Here we discuss the overall shock structure for relatively low σ_e . Figure 3 is the global shock structure at $\omega_{pe}t = 500$ for $\sigma_e = 3 \times 10^{-3}$. The format is the same as Figure 2. A well-developed shock front is distinctly visible at $x/(c/\omega_{pe}) \sim 160$.

The filamentary magnetic field, expected for the structure of the Weibel-generated magnetic field, is seen at the shock front in the x and z direction. In the in-plane configuration, previous works indeed showed that the WI excites B_x as well as B_z (e.g., Matsukiyo & Sc-

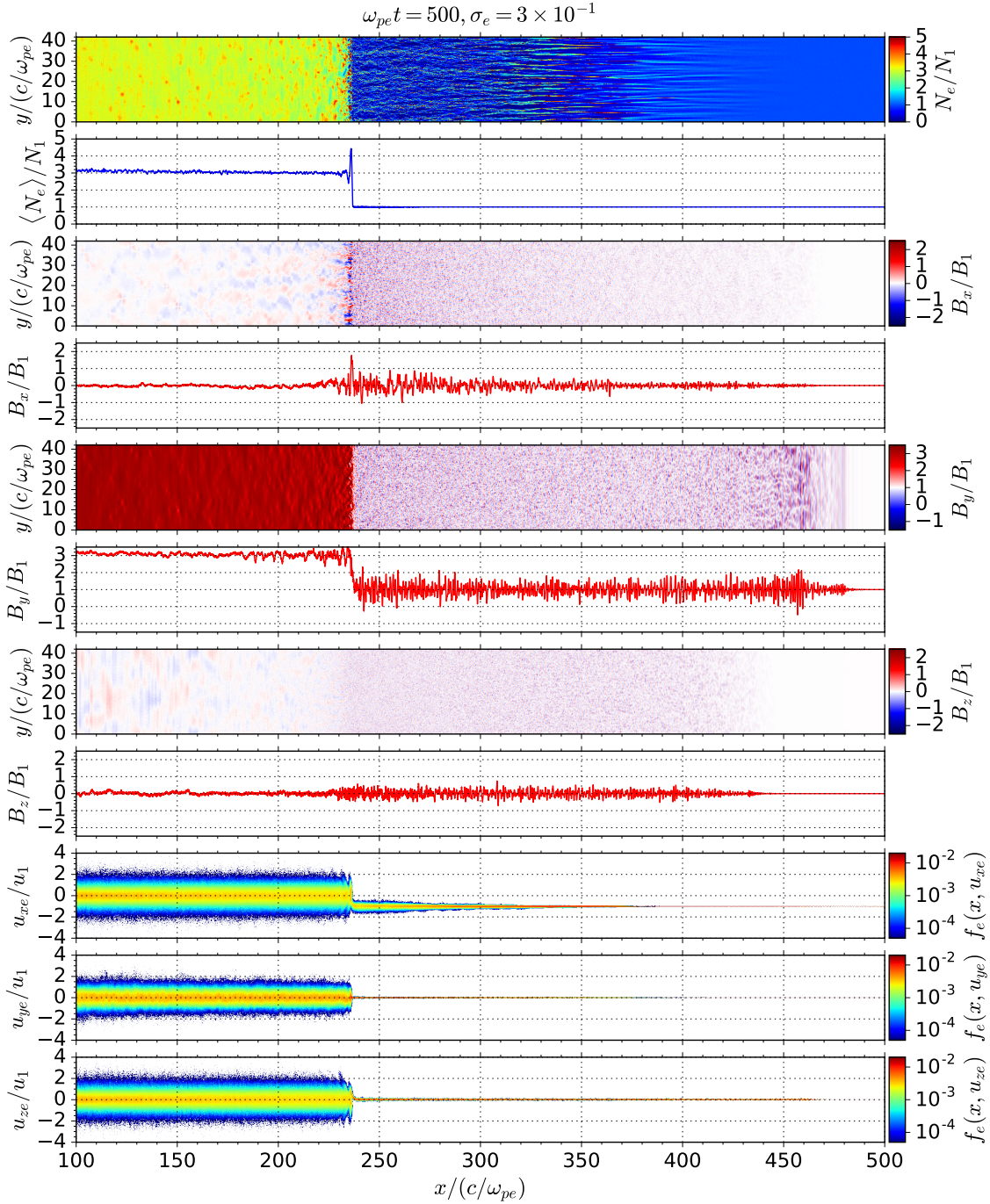


Figure 2. Shock structure and electron phase space from a simulation with $\sigma_e = 3 \times 10^{-1}$ at $\omega_{pet} = 500$. From top to bottom, the electron number density N_e , the average density $\langle N_e \rangle$, the longitudinal magnetic field B_x , 1D cut for B_x along $y/(c/\omega_{pe}) = 21$, the in-plane magnetic field B_y , 1D cut for B_y along $y/(c/\omega_{pe}) = 21$, the out-of-plane magnetic field B_z , 1D cut for B_z along $y/(c/\omega_{pe}) = 21$ and the electron phase-space plots of x - u_{xe} , x - u_{ye} and x - u_{ze} are shown.

holer 2006). Our linear analysis arrives at the same conclusion (see Appendix A). Thus we think that the fluctuations in B_x and B_z near the shock front is attributed to the WI. The maximum magnetic field energies for both components reach about 10%–20% of the

upstream kinetic energy, which is consistent with the previous studies (Kato 2007; Chang et al. 2008; Sironi & Spitkovsky 2011). However, the length of the Weibel filaments are shorter than that in the out-of-plane configuration (see Iwamoto et al. 2017, Figure 3). As we

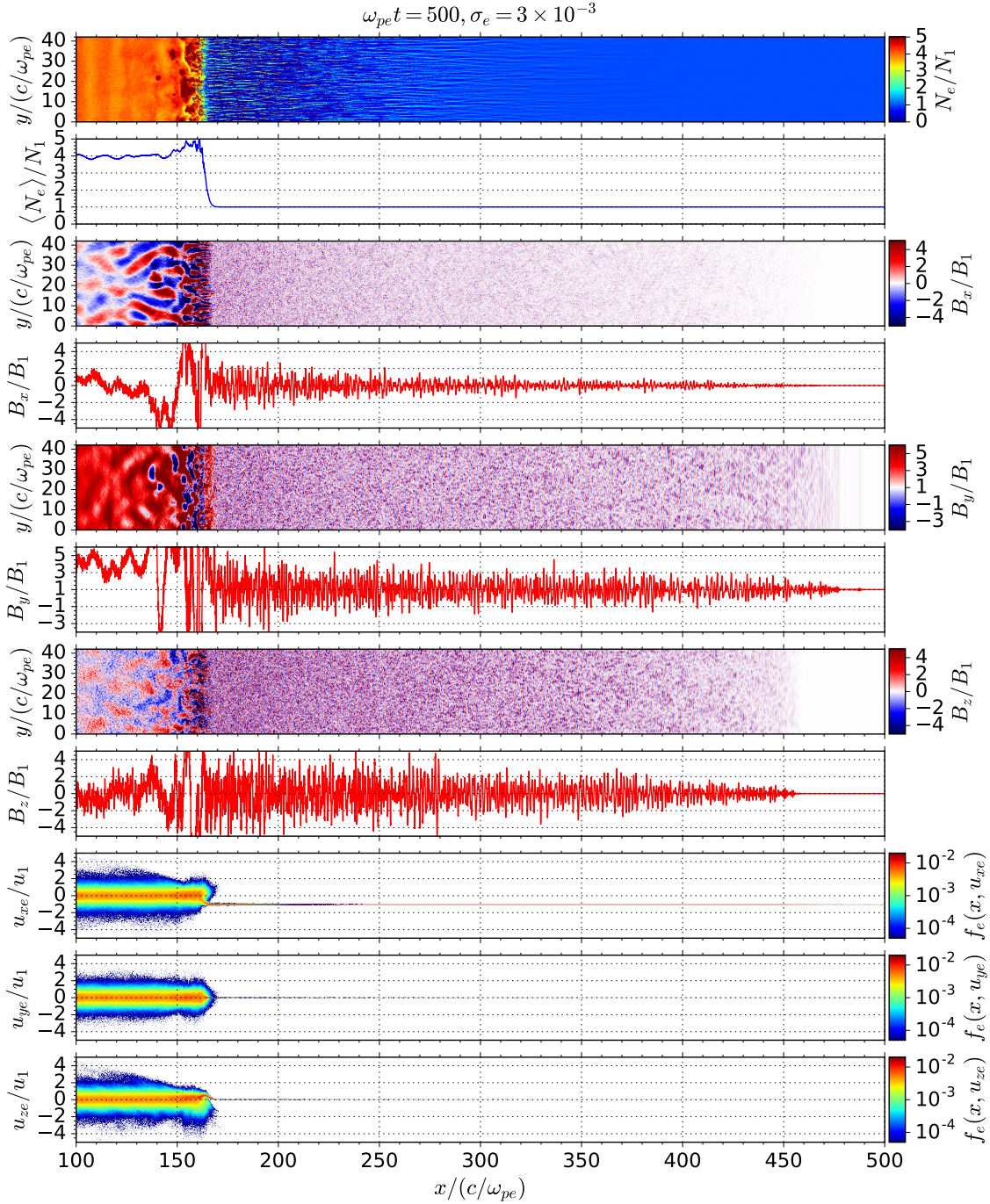


Figure 3. Shock structure and electron phase space from a simulation with $\sigma_e = 3 \times 10^{-3}$ at $\omega_{pe}t = 500$. The format is the same as Figure 2.

already explained, the WI is driven unstable by the effective temperature anisotropy induced by the reflected particles (Kato 2007; Chang et al. 2008). Therefore, the difference of the Weibel filaments originate from the relatively short reflected particle beam in the in-plane configuration.

One of the possible causes for the relatively short reflected particle beam is the relatively strong shock-compressed magnetic field in the in-plane configuration. Recall that the degree of freedom is three in the in-plane configuration. The adiabatic index for a relativistic ideal gas is $4/3$ rather than $3/2$ in the in-plane configuration and thus the compression ratio is greater than that

in the out-of-plane configuration. Since particles are reflected off the shock-compressed magnetic field, the strong magnetic field compared to the out-of-plane case may result in a shorter length for the reflected particle beam.

The suppression of the cross-field diffusion in the in-plane configuration may also contribute to the relatively short reflected particle beam. Jokipii et al. (1993) and Jones et al. (1998) mathematically proved that charged particles cannot move further than one Larmor radius from a given magnetic field if there are one or more ignorable coordinates. A notable exception is a 2D system with the out-of-plane magnetic field, which thus allows particles to diffuse across the magnetic field. In contrast, the diffusion of particles back into the upstream is prohibited in the in-plane configuration. Therefore, the length of the reflected particle beam in the in-plane case may become shorter than that in the out-of-plane case.

The precursor waves are observed both in B_y and B_z and the delay of the O-mode precursor wave is identified in this case as well. The generation time of the O-mode wave may be estimated to be $\omega_{pe}t \sim 40$. The amplitude of the O-mode wave is comparable to that of the X-mode wave unlike the high- σ_e case. The σ_e dependence is discussed in Section 4.4 in more detail. Notice that clear density filaments are observed in the precursor region in this case as well.

4. PRECURSOR WAVE

4.1. Wave Mode

As we mentioned in Section 3, the X-mode and O-mode electromagnetic waves are observed in the in-plane configuration. Both of the waves propagate perpendicular to the ambient magnetic field and are linearly polarized in pair plasmas. The wave magnetic field of the X-mode is parallel to the ambient magnetic field, whereas that of the O-mode is perpendicular.

Figure 4 is the enlarged view of the region in $300 \leq x/(c/\omega_{pe}) \leq 320$ for $\sigma_e = 3 \times 10^{-1}$ (left) and $200 \leq x/(c/\omega_{pe}) \leq 220$ for $\sigma_e = 3 \times 10^{-3}$ (right), and shows the y and z components of the wave electromagnetic fields at $\omega_{pe}t = 500$. The electromagnetic fields are normalized by the upstream ambient magnetic field B_1 . The top panels show the y component of the wave magnetic field δB_y and the z component of the wave electric field δE_z , and the bottom panels show the z component of the wave magnetic field δB_z and the y component of the wave electric field δE_y . The red and blue lines indicate the magnetic field and electric field, respectively. Recall that the upstream ambient magnetic field B_1 is oriented along the y axis. The anticorrelation between δB_y and

δE_z and the correlation between δB_z and δE_y in phase are clearly seen in both cases, and the amplitude of the magnetic field is almost identical to that of the electric field. It is easy to confirm that the waves carry the positive Poynting flux, indicating that the waves propagate toward the $+x$ direction. All these results show that the X-mode and O-mode electromagnetic waves travel upstream.

4.2. Time Evolution

Now we discuss time evolution of the precursor wave power. Figure 5 shows the time evolution of the wave energy from $\omega_{pe}t = 300$ up to $\omega_{pe}t = 500$ for $\sigma_e = 3 \times 10^{-1}$ (left) and $\sigma_e = 3 \times 10^{-3}$ (right). The time evolution is determined by the same method as our previous study (Iwamoto et al. 2017). The wave energy is given in units of the upstream bulk kinetic energy, and y and z components are shown in the solid and dashed lines, respectively. As shown in Figure 4, the amplitude of the electric field is comparable to that of the magnetic field. Thus the same plots for the electric field is almost identical and we here show only those for the magnetic field.

For $\sigma_e = 3 \times 10^{-1}$, although δB_y gradually declines in time, it still remains finite and gets saturated at around $\omega_{pe}t = 460$. In contrast, δB_z shows continuous decrease. Although the O-mode wave emission might be shut off after long-term evolution, the X-mode wave emission has already reached a quasi-steady state by the end of our simulation and the wave amplitude is comparable to that in the out-of-plane configuration (see Section 4.4). Therefore, the coherent electromagnetic precursor wave emission continues in the in-plane as well as out-of-plane configuration.

For $\sigma_e = 3 \times 10^{-3}$, both δB_y and δB_z are already saturated in this time range. Considering that δB_y is the component expected from the linear theory of the SMI, it is somewhat surprising that δB_z is always greater than δB_y . We discuss the σ_e dependence in Section 4.4 in detail.

4.3. Wavenumber Spectra

Figure 6 shows the precursor wave power spectra for each component in wavenumber space normalized by the upstream ambient magnetic field energy density. The left column shows the spectra of δB_y (top) and δB_z (bottom) for $\sigma_e = 3 \times 10^{-1}$, whereas the right column shows the spectra of δB_y (top) and δB_z (bottom) for $\sigma_e = 3 \times 10^{-3}$. The spectra are obtained in the same manner as in our previous study (Iwamoto et al. 2017). Note that the Nyquist wavenumber for our simulation

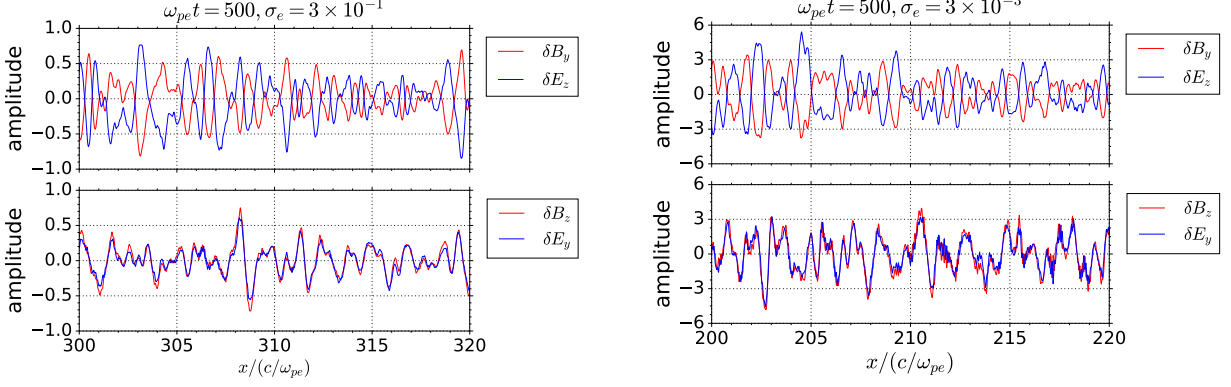


Figure 4. y and z components of wave electromagnetic fields at $\omega_{pe}t = 500$ for $\sigma_e = 3 \times 10^{-1}$ (left) and $\sigma_e = 3 \times 10^{-3}$ (right). The electromagnetic fields are normalized by the upstream ambient magnetic field. The red and blue solid lines indicate the magnetic field and electric field, respectively.

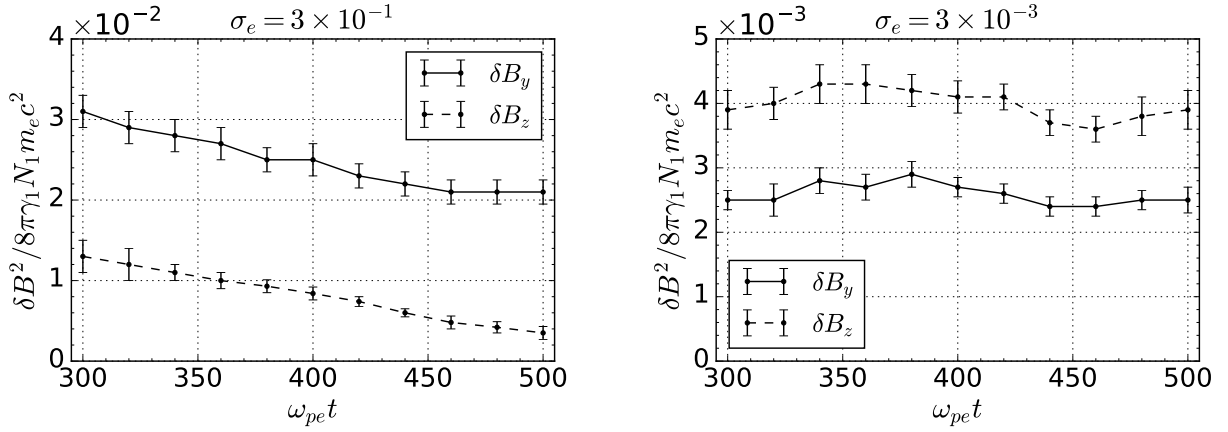


Figure 5. Time evolution of the average wave energy from $\omega_{pe}t = 300$ to $\omega_{pe}t = 500$ for $\sigma_e = 3 \times 10^{-1}$ (left) and $\sigma_e = 3 \times 10^{-3}$ (right). The wave energy is normalized by the upstream bulk kinetic energy. The solid and dashed lines indicate y and z components, respectively.

is $k_N c / \omega_{pe} \simeq 120$ and both X-mode (δB_y) and O-mode (δB_z) precursor waves are well resolved.

The white solid line indicates the theoretical cutoff wavenumber:

$$k_x = \beta_{sh} \gamma_{sh} \sqrt{k_y^2 + \frac{2\omega_{pe}^2}{c^2}}, \quad (4)$$

where β_{sh} is the shock velocity normalized by the speed of light and γ_{sh} is the Lorentz factor of the shock velocity (see Iwamoto et al. 2017, Appendix B). This theoretical cutoff wavenumber comes from the wavenumber below which the group velocity of the precursor wave is smaller than the shock velocity. Therefore, only those waves with k_x greater than the threshold can escape from the shock toward upstream. The dispersion relation of the X-mode in a cold magnetized pair plasma is used to derive Equation 4. For γ_1 and σ_e used in our simulation, the dispersion relation in the simulation frame can be

written as

$$\omega^2 \simeq 2\omega_{pe}^2 + k^2 c^2. \quad (5)$$

This dispersion relation is identical to that of the O-mode in a cold pair plasma, and we use Equation 4 for the O-mode wave as well. The shock propagation velocity is determined from the time evolution of the y -averaged electron number density $\langle N_e \rangle$, which is then used for calculation of the theoretical cutoff wavenumber. The result shows that the precursor waves are indeed propagating away from the shock, suggesting that they are generated at the shock front.

4.4. σ_e Dependence

Now we discuss the σ_e dependence of the precursor wave amplitude. The wave amplitude was calculated by integrating the power spectra (Figure 6) over the whole wavenumber space. Figure 7 shows the precursor wave energy as a function of σ_e normalized by the upstream ambient magnetic field energy (left) and the upstream

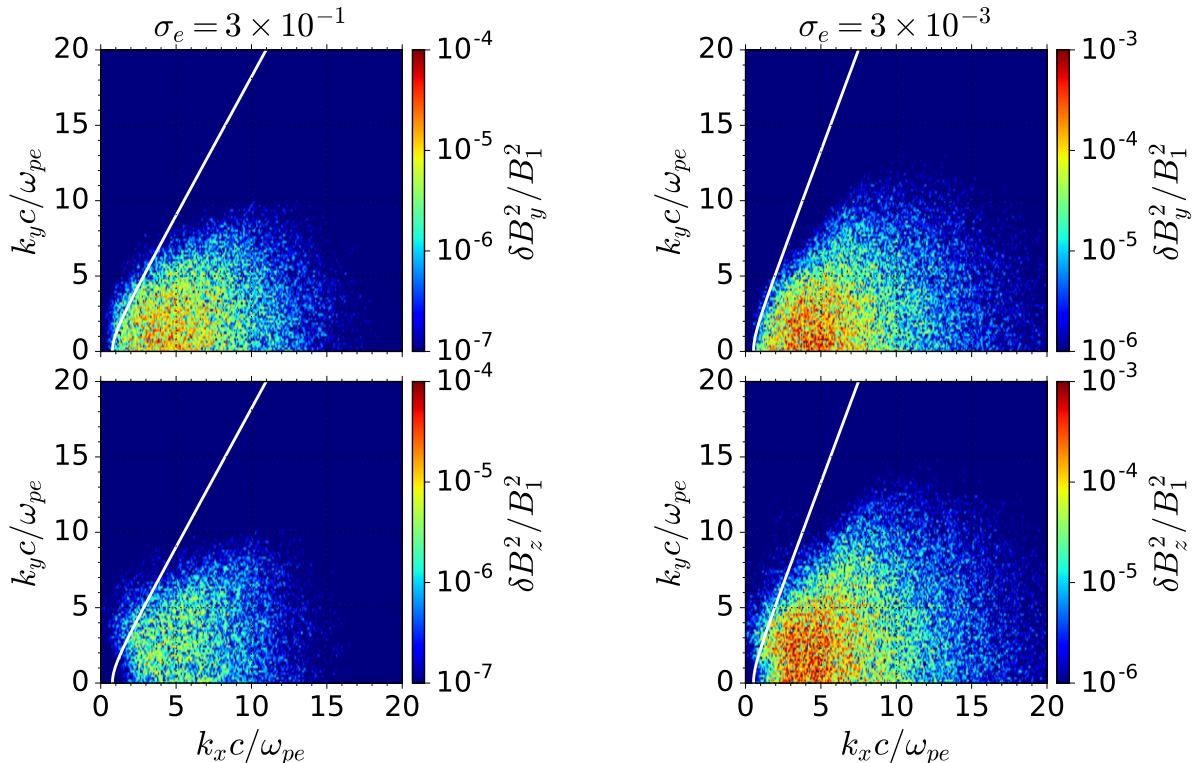


Figure 6. Wavenumber power spectra of the wave magnetic field intensity for each component at $\omega_{pe}t = 500$. The left and right column shows the spectra for $\sigma_e = 3 \times 10^{-1}$ and $\sigma_e = 3 \times 10^{-3}$, respectively. A theoretical cutoff wavenumber is also shown in the white line.

bulk kinetic energy (right). The latter may be understood as the energy conversion rate from the upstream bulk kinetic energy to the precursor wave energy. The red, blue and magenta indicate the X-mode wave energy δB_y^2 , O-mode wave energy δB_z^2 and total wave energy $\delta B_y^2 + \delta B_z^2$, respectively. The simulation results in the out-of-plane configuration by [Iwamoto et al. \(2017\)](#) is also shown in green for comparison. Note that only the X-mode precursor waves (δB_z) are excited in the out-of-plane configuration.

For $\sigma_e \gtrsim 10^{-2}$, the X-mode wave energy δB_y^2 in the in-plane configuration shows the same tendency as that in the out-of-plane configuration. This may be understood as follows. The ambient magnetic field is larger than the magnetic field fluctuations generated by the instability in the shock-transition region and almost unperturbed for high σ_e . Thus the X-mode wave excitation via the SMI is nearly identical between the in-plane and out-of-plane configurations.

For $\sigma_e \lesssim 10^{-2}$, the X-mode wave energy δB_y^2 in the in-plane configuration is greater than that in the out-of-plane configuration. This may be explained in terms of the coherence of the particle gyromotion in the shock-transition region. The WI generates strong magnetic field fluctuations for low σ_e and the shock-transition

region is dominated by the Weibel-generated magnetic field in both of the configurations. While charged particles, on average, gyrate in the $x-z$ plane for the in-plane configuration, they always gyrate in the $x-y$ plane for the out-of-plane configuration. Since the z direction is ignored in our 2D simulations, the particle gyromotion in the in-plane case is less perturbed by the Weibel-generated turbulence than that in the out-of-plane case. In the in-plane case, therefore, the electromagnetic wave emission may be sufficiently amplified by the SMI and the wave amplitude may grow larger than that in the out-of-plane case.

The O-mode wave energy δB_z^2 is smaller than the X-mode wave energy δB_y^2 for $\sigma_e \gtrsim 10^{-2}$, whereas it exceeds the X-mode for $\sigma_e \lesssim 10^{-2}$. This tendency cannot be explained by the above argument. We discuss a possible excitation mechanism of O-mode waves and its relation to the σ_e dependence in Section 5.1 in detail.

In conclusion, the simulation results have demonstrated that regardless of the orientation of the upstream ambient magnetic field, the precursor waves remain finite amplitude and coherent in 2D. This is true even for relatively low σ_e cases where the WI grows into substantial amplitude in the shock-transition region. The results confirm the idea that the coherent electromag-

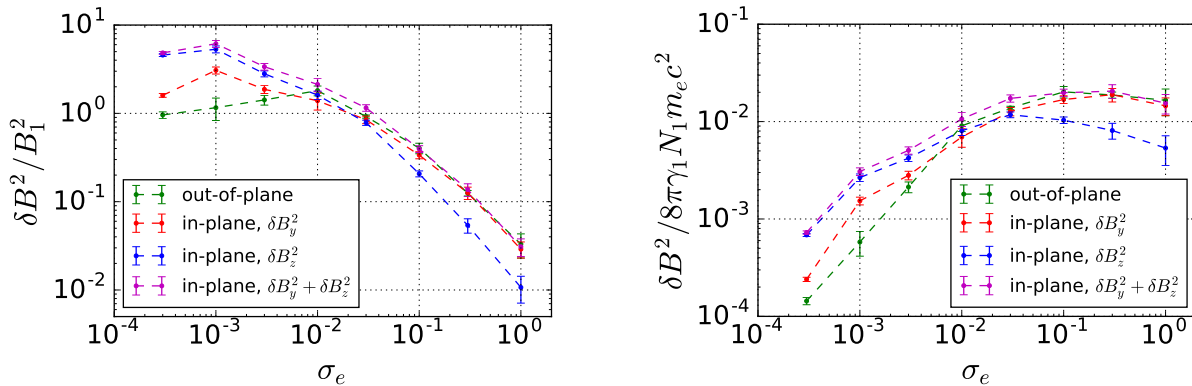


Figure 7. Energy of the precursor wave emission given in units of the ambient upstream magnetic field energy (left) and the upstream kinetic energy (right) as a function of σ_e . The red, blue and magenta indicate δB_y^2 , δB_z^2 and $\delta B_y^2 + \delta B_z^2$, respectively. The simulation results by [Iwamoto et al. \(2017\)](#) are shown in green.

netic precursor wave emission is the real nature of the relativistic magnetized shocks.

5. DISCUSSION

5.1. Excitation Mechanism of O-mode Waves

Our simulation results show that the O-mode as well as X-mode electromagnetic waves are excited in relativistic shocks. As we already mentioned, the linear theory of the SMI ([Wu & Lee 1979](#); [Lee et al. 1980](#); [Melrose et al. 1982, 1984](#)) predicts that the X-mode wave emission overwhelms the O-mode wave emission. However, in the in-plane configuration, the O-mode precursor wave is clearly identified in the upstream region. This may be explained qualitatively as follows.

In the early stage of the simulation, the ambient magnetic field in the shock transition is entirely oriented along the y axis. Charged particles gyrate in the x - z plane and induce the SMI. Since the X-mode wave has a fluctuating component of the magnetic field parallel to the ambient magnetic field, only δB_y is excited in this stage. When the fluctuations in B_z generated by the plasma instabilities in the shock-transition region have grown to be a non-negligible fraction of the ambient magnetic field, the net ambient magnetic field in the shock-transition region is undulated in the y - z plane. If the SMI is induced by particles gyrating around the net ambient magnetic field, the X-mode wave in the shock-transition region will have δB_z as well as δB_y . Such a X-mode wave experiences changes in the direction of the ambient magnetic field during its propagation toward upstream. If the polarization of the wave electromagnetic field remains unchanged during the propagation, the X-mode wave may be mode-converted into an O-mode wave in the upstream. By performing simple PIC simulations, we have confirmed that this hypothesis is indeed correct. That is, a X-mode wave keeps its polar-

ization and is converted into an O-mode as it propagates through a layer of magnetic field rotation. Therefore, we believe that O-mode waves observed in the precursor region are the result of mode conversion from the X-mode generated by the SMI in the turbulent shock-transition region.

The delay of the O-mode wave in our simulation provides indirect evidence for this model. The excitation mechanism shows that the O-mode wave is excited after the generation of the strong magnetic field fluctuations by the instabilities in the shock-transition region. In fact, the generation time of the O-mode waves ($\omega_{pe} t \sim 80$ for $\sigma_e = 3 \times 10^{-1}$ and $\omega_{pe} t \sim 40$ for $\sigma_e = 3 \times 10^{-3}$) is roughly identical to the saturation time of the plasma instabilities (see [Appendix A](#)).

The σ_e dependence of the O-mode wave amplitude in [Figure 7](#) may be explained by this excitation mechanism. For $\sigma_e \gtrsim 10^{-2}$, the ambient magnetic field is much larger than the magnetic field fluctuations and almost aligned in the y direction. Thus δB_y should be the main component of the X-mode wave in the shock-transition region, and δB_z which is observed as the O-mode wave in the upstream region may be much smaller for high σ_e .

For $\sigma_e \lesssim 10^{-2}$, the Weibel-generated magnetic field dominates over the ambient magnetic field and the effective σ_e becomes much larger in the shock-transition region. The higher effective σ_e allows a wave generated via a lower-order cyclotron harmonic resonance n to satisfy the condition $\omega = n\omega_{ce} \gtrsim \sqrt{2(1 + \beta_{sh}\gamma_{sh})}\omega_{pe}$ such that it can propagate upstream (see [Iwamoto et al. 2017](#)). We think that the lower cyclotron harmonics contribution may be the reason for the enhanced power of δB_z . In other words, the Weibel-generated magnetic field plays the role for the enhanced O-mode wave power. This model indicates that the O-mode wave continues to exist with a finite amplitude for considerably lower σ_e .

5.2. Implication for 3D

Based on the 2D simulation results obtained with both the in-plane and out-of-plane configurations, we now discuss implication for three-dimensional (3D) systems. As discussed in Section 5.1, the O-mode precursor wave emission is attributed to the large-amplitude magnetic field fluctuations generated in the shock-transition region, in particular by the WI at low σ_e . Since we can naturally expect the presence of such fluctuations in 3D, the O-mode precursor waves will also be excited. It is, however, not easy to estimate the relative emission efficiency between the O-mode and X-mode. Since the particle gyromotion in 3D should be less coherent than the 2D with the in-plane configuration, the O-mode wave power will become smaller. Concerning the gyromotion in the shock-transition region, the out-of-plane configuration may better represent 3D.

We have found that the particle acceleration efficiency also depends on the magnetic field configuration. Non-thermal particles are not generated in the in-plane configuration in 2D (see Appendix B), whereas a clear non-thermal tail is observed in the energy spectra for low σ_e in the out-of-plane configuration (see [Iwamoto et al. 2017](#), Figure 10). Considering the suppression of the cross-field diffusion in the in-plane configuration, again the out-of-plane configuration may be closer to 3D concerning the particle acceleration efficiency.

In any case, the important fact is that the intense coherent precursor wave can be excited for a wide range of σ_e in both of the configurations. This strongly indicates that the intense coherent precursor wave emission is intrinsic to relativistic magnetized shocks and even in 3D.

5.3. Implication for WFA in Relativistic Shocks

Now we discuss the feasibility of the WFA in relativistic shocks. The WFA requires an intense electromagnetic wave in the sense that the wave strength parameter $a = e\delta E/m_e c\omega$ is greater than unity, where δE is the amplitude of the wave electric field and ω is the wave frequency ([Kuramitsu et al. 2008](#)). We estimated the strength parameter of the precursor wave with two different methods; one based on the oscillation amplitude of the transverse particle velocity, the other based on the wave amplitude. The details can be found in our previous paper ([Iwamoto et al. 2017](#)) except that the total wave power $\sqrt{\delta B_y^2 + \delta B_z^2}$ is used here. The results are shown in Figure 8 which demonstrates that the amplitudes of the precursor waves are indeed quite large.

Assuming a linear scaling of the strength parameter with respect to the Lorentz factor γ_1 (see, e.g., [Hoshino](#)

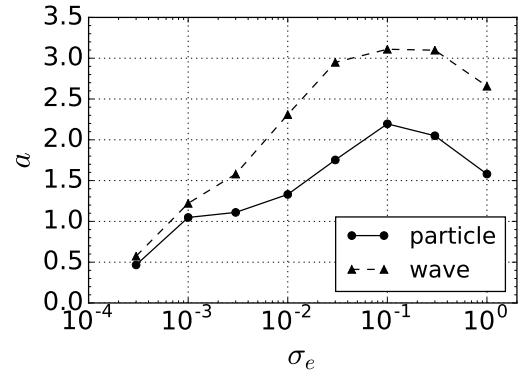


Figure 8. Strength parameter of the precursor wave as a function of σ_e . The solid and dashed line indicate the estimation method based on the particle quiver velocity and the wave amplitude, respectively.

[2008](#)), we may estimate the region in the σ_e - γ_1 parameter space where the WFA is effective. In Figure 9, the solid and dashed line indicates the estimates obtained by using the simulation results for the out-of-plane and in-plane configuration, respectively. This clearly indicates that higher Lorentz factors and moderate magnetizations are favorable for the WFA model. Again, we draw the same conclusion as [Iwamoto et al. \(2017\)](#) that highly relativistic external shocks of GRBs are candidate sites for acceleration of ultra-high-energy cosmic rays.

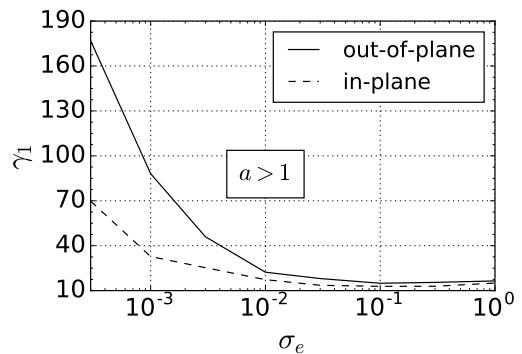


Figure 9. Parameter space plot in σ_e and γ_1 . The solid and dashed line indicates the out-of-plane and in-plane case, respectively. Strength parameter a is greater than unity in the region above each line.

The above discussion primarily focused on the wave amplitude. Although the large-amplitude precursor waves will induce wakefield in ion–electron plasmas, it is not clear yet whether the wakefield can sufficiently accelerate particles. The previous study demonstrated the WFA using Gaussian laser pulse ([Kuramitsu et al. 2008](#)). However, the actual precursor waves are a super-

position of waves continuously emitted from different positions in the shock front, and the spectra are rather broadband in wavenumber as shown in Figure 6. A ponderomotive force exerted by such waves should become weaker (e.g., [Kruer 1988](#); [Hoshino 2008](#)). Therefore, the generation of wakefield and particle acceleration may be less efficient. Also, different properties of the WI in pair and ion-electron plasmas, energy exchange between ions and electrons (e.g., [Kumar et al. 2015](#)) may influence the efficiency of the particle acceleration. These issues should be examined by performing shock simulations in ion-electron plasmas in the future.

6. SUMMARY

In this work, we performed 2D simulations of relativistic perpendicular shocks in pair plasmas with the in-plane ambient magnetic field, and investigated the physics of the intense coherent precursor wave emission. In the in-plane configuration, O-mode as well as X-mode electromagnetic precursor waves are excited. We think that the O-mode waves are initially excited as X-mode by the SMI in the shock-transition region. Since the instabilities in the shock-transition region generate fluctuations in B_z and disturb the ambient magnetic field, the SMI should excite X-mode waves which have δB_z as well as δB_y . The generated waves having δB_z may be mode-converted into O-mode during the propagation to the upstream region. The delay of the O-mode wave identified in our simulation is consistent with this model. We quantified the precursor wave amplitude as a func-

tion of the magnetization parameter σ_e and compared the simulation results with that in the out-of-plane configuration by [Iwamoto et al. \(2017\)](#). The wave amplitude is sufficiently large to disturb the upstream plasma even in the Weibel-dominated regime and the transverse density filaments are generated as in the case of the out-of-plane configuration. We thus conclude that the precursor wave emission is the real nature of the realistic magnetized shocks.

In the range of σ_e used in our simulations, the precursor wave keeps coherent and its amplitude is large enough to induce the wakefield. Therefore, the WFA may operate in relativistic ion-electron shocks.

We are grateful to Jacek Niemiec, Martin Pohl, Oleh Kobzar, Arianna Ligorini and Artem Bohdan for fruitful discussion.

Numerical computations and analyses were in part carried out on Cray XC30 and computers at Center for Computational Astrophysics, National Astronomical Observatory of Japan.

This work used the computational resources of the K computer provided by the RIKEN Advanced Institute for Computational Science through the HPCI System Research Project (Project ID: hp150263), and was supported in part by JSPS KAKENHI Grant Number 17H02877

This work also used the computational resources of the HPCI system provided by Information Technology Center, Nagoya University through the HPCI System Research Project (Project ID: hp170158).

APPENDIX

A. ELECTROMAGNETIC INSTABILITIES IN SHOCK-TRANSITION REGION

Here we present linear analysis of the electromagnetic instabilities excited in the shock-transition region. The dispersion relation for electromagnetic waves propagating parallel to an ambient magnetic field is given by (see, e.g., [Yoon & Davidson 1987](#))

$$D(k, \omega) = 1 - \frac{c^2 k^2}{\omega^2} + \sum_s \frac{\Omega_{ps}^2}{\omega^2} \int_{-\infty}^{\infty} \int_0^{\infty} \frac{(\gamma\omega - ck_{\parallel}) \partial F_{0s} / \partial u_{\perp} + ck_{\perp} \partial F_{0s} / \partial u_{\parallel}}{\gamma\omega \pm \Omega_{cs} - ck_{\parallel}} \frac{\pi u_{\perp}^2}{\gamma} du_{\perp} du_{\parallel}, \quad (\text{A1})$$

where $\gamma = \sqrt{1 + u_{\perp}^2 + u_{\parallel}^2}$ is the Lorentz factor, Ω_{ps} is the non-relativistic plasma frequency, Ω_{cs} is the non-relativistic cyclotron frequency and F_{0s} is the unperturbed distribution function normalized as follows:

$$\int_{-\infty}^{\infty} \int_0^{\infty} F_{0s}(u_{\parallel}, u_{\perp}) 2\pi u_{\perp} du_{\perp} du_{\parallel} = 1. \quad (\text{A2})$$

The subscript s indicates particle species (i.e., electron and positron). In Equation A1, the positive (negative) sign corresponds to the right-hand (left-hand) polarization.

We assume a cold ring distribution for both electrons and positrons,

$$F_{0s} = \frac{1}{2\pi u_{0s}} \delta(u_{\perp} - u_{0s}) \delta(u_{\parallel}). \quad (\text{A3})$$

By substituting Equation A3 for Equation A1, we obtain

$$D(k, \omega) = 1 - \frac{c^2 k^2}{\omega^2} - \sum_s \frac{\omega_{ps}^2}{\omega(\omega \pm \omega_{cs})} + \frac{1}{2} \left(1 - \frac{c^2 k^2}{\omega^2}\right) \sum_s \left(1 - \frac{1}{\gamma_{0s}^2}\right) \frac{\omega_{ps}^2}{(\omega \pm \omega_{cs})^2}, \quad (\text{A4})$$

where $\gamma_{0s} = \sqrt{1 + u_{0s}^2}$ is the initial Lorentz factor, $\omega_{ps} = \Omega_{ps}/\sqrt{\gamma_{0s}}$ is the relativistic plasma frequency and $\omega_{cs} = \Omega_{cs}/\gamma_{0s}$ is the relativistic cyclotron frequency. When $\gamma_{0s} = 1$, Equation A4 is identical to the dispersion relation in a cold magnetized plasma. Introducing $\omega_{pe} \equiv \omega_{pe^-} = \omega_{pe^+}$ and $\omega_{ce} \equiv -\omega_{ce^-} = \omega_{ce^+} > 0$, Equation A4 reduces

$$D(k, \omega) = 1 - \frac{c^2 k^2}{\omega^2} - \frac{2\omega_{pe}^2}{\omega^2 - \omega_{ce}^2} + \beta_0^2 \left(1 - \frac{c^2 k^2}{\omega^2}\right) \frac{\omega_{pe}^2 (\omega^2 + \omega_{ce}^2)}{(\omega^2 - \omega_{ce}^2)^2}, \quad (\text{A5})$$

where $\beta_0 = u_{0e\pm}/\gamma_{0e\pm}$. $D(k, \omega) = 0$ is expressed as follows:

$$\left(\frac{\omega}{\omega_{pe}}\right)^6 - \left(\frac{c^2 k^2}{\omega_{pe}^2} + 2\sigma_e - \beta_0^2 + 2\right) \left(\frac{\omega}{\omega_{pe}}\right)^4 + \left[(2\sigma_e - \beta_0^2) \frac{c^2 k^2}{\omega_{pe}^2} + \sigma_e(\sigma_e + \beta_0^2 + 2)\right] \left(\frac{\omega}{\omega_{pe}}\right)^2 - \sigma_e(\sigma_e + \beta_0^2) \frac{c^2 k^2}{\omega_{pe}^2} = 0, \quad (\text{A6})$$

where $\sigma_e = \omega_{ce}^2/\omega_{pe}^2$. In this linear analysis, we assume that the wavenumber k is a real number and consider only the region where $k \geq 0$ and $\omega \geq 0$ because of the symmetry of k and ω for a pair plasma.

First, we study the case of $\sigma_e > (2 - \beta_0^2)^2/8\beta_0^2$. ω becomes a complex number at $k \leq k_1$ and $k \geq k_2$. Here, the threshold wavenumber k_1 and k_2 are determined from

$$\left(\frac{ck_1}{\omega_{pe}}\right)^2 = f\left(\frac{\omega_1^2}{\omega_{pe}^2}\right), \quad (\text{A7})$$

$$\left(\frac{ck_2}{\omega_{pe}}\right)^2 = f\left(\frac{\omega_2^2}{\omega_{pe}^2}\right), \quad (\text{A8})$$

$$k_1 < k_2, \quad (\text{A9})$$

$$f(x) = x - 2 - \frac{2(\sigma_e - \beta_0^2)x - 2\sigma_e(\sigma_e + \beta_0^2)}{x^2 - (2\sigma_e - \beta_0^2)x + \sigma_e(\sigma_e + \beta_0^2)}. \quad (\text{A10})$$

ω_1 and ω_2 satisfy

$$f'\left(\frac{\omega_1^2}{\omega_{pe}^2}\right) = f'\left(\frac{\omega_2^2}{\omega_{pe}^2}\right) = 0, \quad (\text{A11})$$

$$\omega_1 > \omega_2. \quad (\text{A12})$$

Figure 10 shows the dispersion relation with $\sigma_e = 0.3, \gamma_0 = 40$ numerically obtained from Equation A6. The real and imaginary part of the frequency is shown by the solid and dashed line, respectively. The unstable branch for $k \leq k_1$ and $k \geq k_2$ is connected to the electromagnetic and Alfvén mode branch, respectively. We think the unstable mode for $k \geq k_2$ corresponds to the Alfvén-ion-cyclotron instability in ion–electron plasmas. The growth rate of the mode $k \leq k_1$ has its maximum at $k = 0$,

$$\frac{\text{Re}(\omega_{max})}{\omega_{pe}} = \sqrt{\frac{1}{2}\sigma_e - \frac{1}{4}\beta_0^2 + \frac{1}{2} + \frac{1}{2}\sqrt{\sigma_e(\sigma_e + \beta_0^2 + 2)}}, \quad (\text{A13})$$

$$\frac{\text{Im}(\omega_{max})}{\omega_{pe}} = \sqrt{-\frac{1}{2}\sigma_e + \frac{1}{4}\beta_0^2 - \frac{1}{2} + \frac{1}{2}\sqrt{\sigma_e(\sigma_e + \beta_0^2 + 2)}}. \quad (\text{A14})$$

The maximum growth rate of the mode $k \geq k_2$ occurs for $ck/\omega_{pe} \gg 1$,

$$\frac{\text{Re}(\omega_{max})}{\omega_{pe}} = \sqrt{\frac{1}{2}\sigma_e - \frac{1}{4}\beta_0^2 + \frac{1}{2}\sqrt{\sigma_e(\sigma_e + \beta_0^2)}}, \quad (\text{A15})$$

$$\frac{\text{Im}(\omega_{max})}{\omega_{pe}} = \sqrt{-\frac{1}{2}\sigma_e + \frac{1}{4}\beta_0^2 + \frac{1}{2}\sqrt{\sigma_e(\sigma_e + \beta_0^2)}}. \quad (\text{A16})$$

If $\sigma_e \gg 1$, then the maximum growth rates for both modes are written as follows:

$$\text{Re}(\omega_{max}) \sim \omega_{ce}, \quad (\text{A17})$$

$$\text{Im}(\omega_{max}) \sim \frac{\beta_0}{\sqrt{2}} \omega_{pe}. \quad (\text{A18})$$

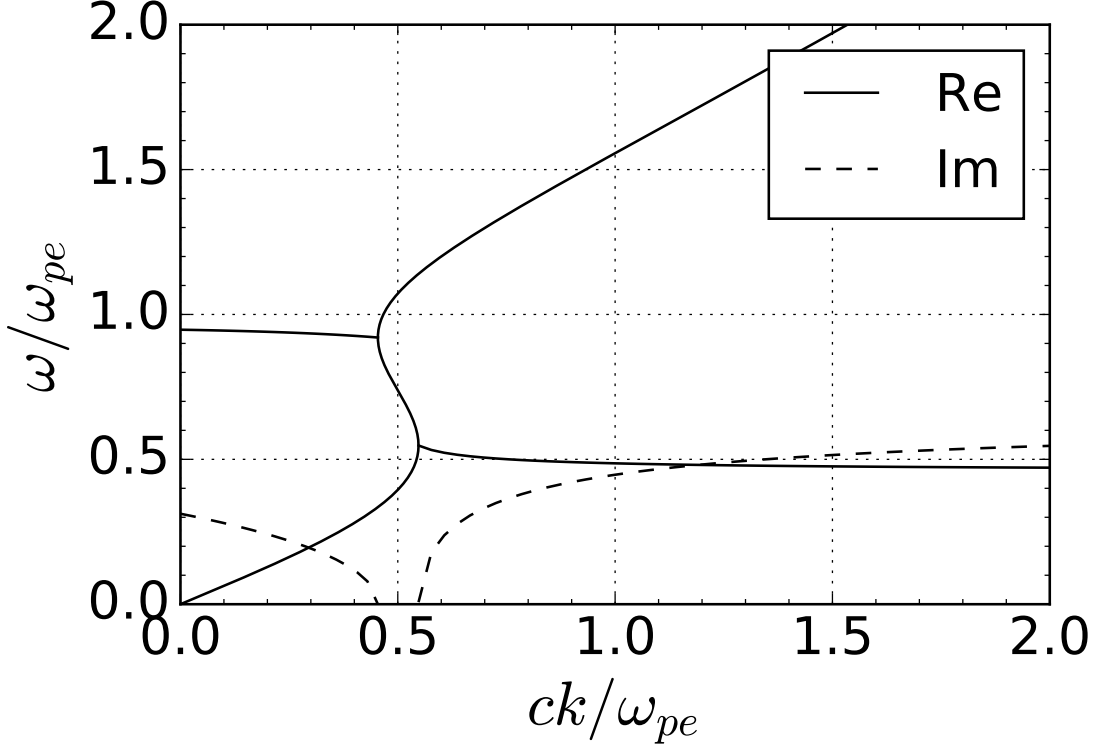


Figure 10. Dispersion relation for $\sigma_e = 0.3$ and $\gamma_0 = 40$. The solid and dashed line indicates the real and imaginary part of the frequency, respectively.

Second, we study the case of $\beta_0^2/8 \leq \sigma_e \leq (2 - \beta_0^2)^2/8\beta_0^2$. For highly relativistic plasma $\beta_0 \sim 1$, the condition is satisfied within a very narrow range of σ_e . In this case, only the instability on the Alfvén mode branch exists at $k \geq k_2$. The dispersion relation is shown in Figure 11. The maximum growth rate is identical to Equation A15 and A16.

Finally, we study the case of $\sigma_e < \beta_0^2/8$. ω is a complex number and a pure imaginary number for $k_2 \leq k < k_3$ and $k \geq k_3$, respectively. Here, the threshold wavenumber k_3 is determined by

$$\left(\frac{ck_3}{\omega_{pe}}\right)^2 = f\left(\frac{\omega_3^2}{\omega_{pe}^2}\right). \quad (\text{A19})$$

The threshold frequency ω_3 satisfies

$$f'\left(\frac{\omega_3^2}{\omega_{pe}^2}\right) = 0, \quad (\text{A20})$$

$$\omega_- < \text{Im}(\omega_3) < \omega_+, \quad (\text{A21})$$

$$\text{Re}(\omega_3) = 0, \quad (\text{A22})$$

where

$$\frac{\omega_{\pm}}{\omega_{pe}} = \sqrt{-\sigma_e + \frac{1}{2}\beta_0^2 \pm \frac{1}{2}\beta_0\sqrt{\beta_0^2 - 8\sigma_e}}. \quad (\text{A23})$$

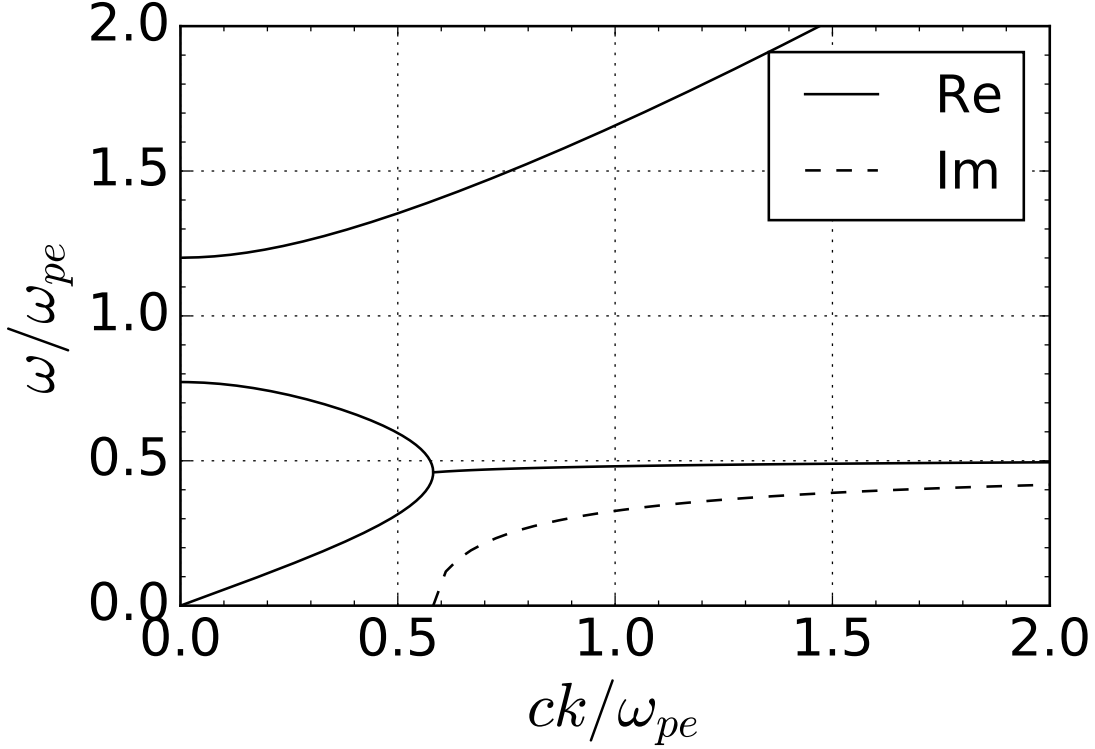


Figure 11. Dispersion relation for $\sigma_e = 0.3$ and $\gamma_0 = 2$.

Figure 12 shows the dispersion relation with $\sigma_e = 3 \times 10^{-3}$, $\gamma_0 = 40$. For $\sigma_e \leq \beta_0^2/8$, there are two purely growing modes when the wavenumber is greater than the threshold wave number k_3 . We think the upper unstable branch corresponds to the WI. The growth rates of these modes asymptotically approach ω_{\pm} as the wavenumber increases. The maximum growth rate is expressed as follows:

$$\text{Im}(\omega_{max}) \sim \omega_+. \quad (\text{A24})$$

If $\sigma_e \ll \beta_0^2$, then the maximum growth rate is written as follows:

$$\text{Im}(\omega_{max}) \sim \beta_0 \omega_{pe}. \quad (\text{A25})$$

We now compare our simulation results with the maximum linear growth rate. Our linear analysis indicates that the electromagnetic fields perpendicular to the ambient magnetic field are induced by the electromagnetic instabilities. In fact, previous simulations showed that the instabilities in the shock-transition region excite B_x as well as B_z in the in-plane configuration (e.g., Winske & Quest 1988; Matsukiyo & Scholer 2006). The maximum values of the x and z components of the magnetic field energy averaged over y axis are determined for each snapshot, and are shown in Figure 13 for $\sigma_e = 3 \times 10^{-1}$ (left) and $\sigma_e = 3 \times 10^{-3}$ (right). The red and blue solid line indicate the x and z component of the magnetic field energy, respectively. The magnetic field energy $\epsilon_B = B^2/8\pi N_1 m_e c^2$ are expressed in units of the upstream kinetic energy. The maximum linear growth rate determined by Equation A16 and Equation A24 is also shown in Figure 13 with the black dashed lines.

For $\sigma_e = 3 \times 10^{-1}$, although the maximum linear growth rate is consistent with the simulation result, it is difficult to differentiate which instabilities generate the magnetic field fluctuations because the maximum growth rates (Equation A16 and A24) are almost the same. Furthermore, our analysis assumes a cold ring distribution and ignores possible kinetic effects that should become important at relatively short wavelength. In any case, we think that the instabilities excited in the shock-transition region generate the magnetic field fluctuations in our simulation.

For $\sigma_e = 3 \times 10^{-3}$, the maximum linear growth rate gives good agreement with the simulation result. In addition, the maximum energy of the fluctuating magnetic field saturates about 10%–20% of the upstream bulk kinetic energy.

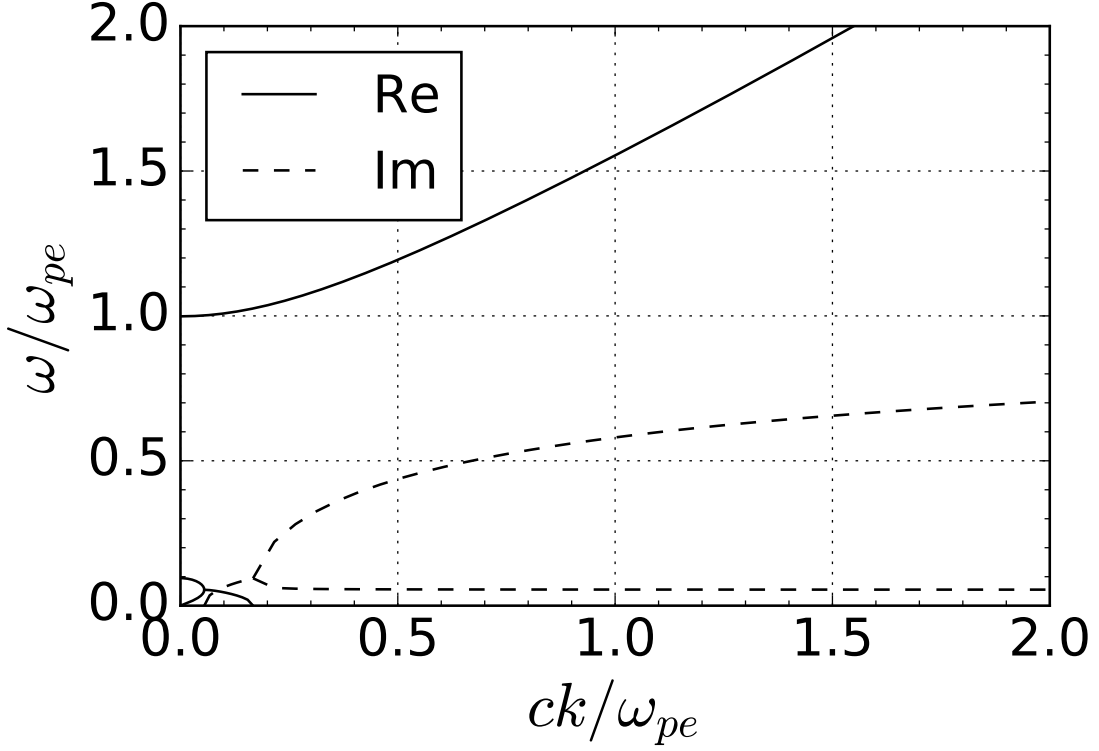


Figure 12. Dispersion relation for $\sigma_e = 3 \times 10^{-3}$ and $\gamma_0 = 40$.

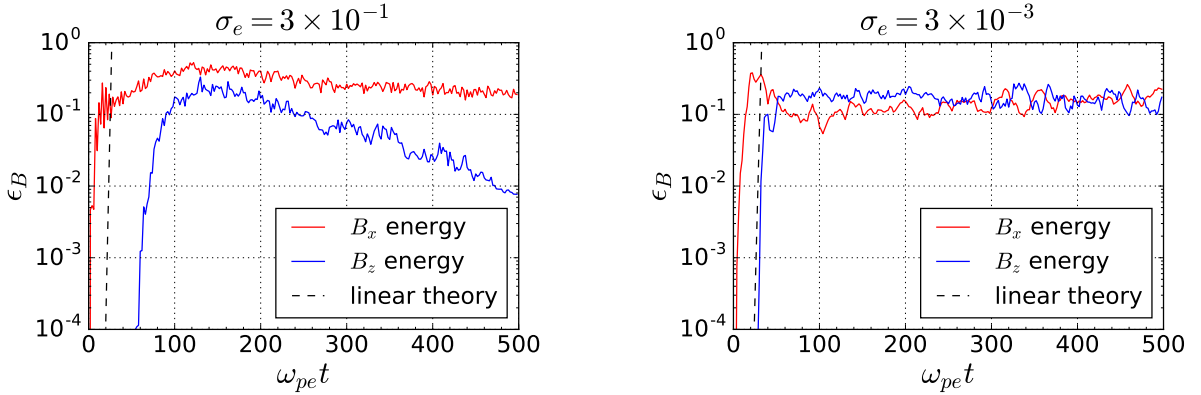


Figure 13. Time evolution of the fluctuating magnetic field energy normalized by the upstream bulk kinetic energy for $\sigma_e = 3 \times 10^{-1}$ (left) and $\sigma_e = 3 \times 10^{-3}$ (right). The red and blue solid lines indicate B_x and B_z energy, respectively. The prediction from the linear theory is also shown by the dashed line.

This result is consistent with the previous studies (Kato 2007; Chang et al. 2008; Sironi & Spitkovsky 2011). Therefore, we conclude that the fluctuations in B_x and B_z in the shock-transition region result from the WI.

B. PARTICLE ENERGY SPECTRA

Figure 14 shows the downstream energy spectra of electrons for $\sigma_e = 3 \times 10^{-1}$ and 3×10^{-3} , which are normalized as follows:

$$\int_1^{\infty} f_e(\gamma) d\gamma = 1. \quad (\text{B26})$$

The energy spectra of positrons are identical to those of electrons. We followed the time evolution from $\omega_{pe}t = 100$ up to $\omega_{pe}t = 500$. For both σ_e , the measured distribution reaches a steady state by the end of our simulation. The energy spectra can be well-fitted with 3D relativistic Maxwellian,

$$f(\gamma)d\gamma \propto \gamma\sqrt{\gamma^2 - 1} \exp\left(-\frac{\gamma mc^2}{kT}\right). \quad (\text{B27})$$

Note that the degree of freedom is three in the in-plane configuration. The fitting result indicates that the downstream particles are completely thermalized. A clear suprathermal tail is not observed in the range of σ_e used in our simulations.

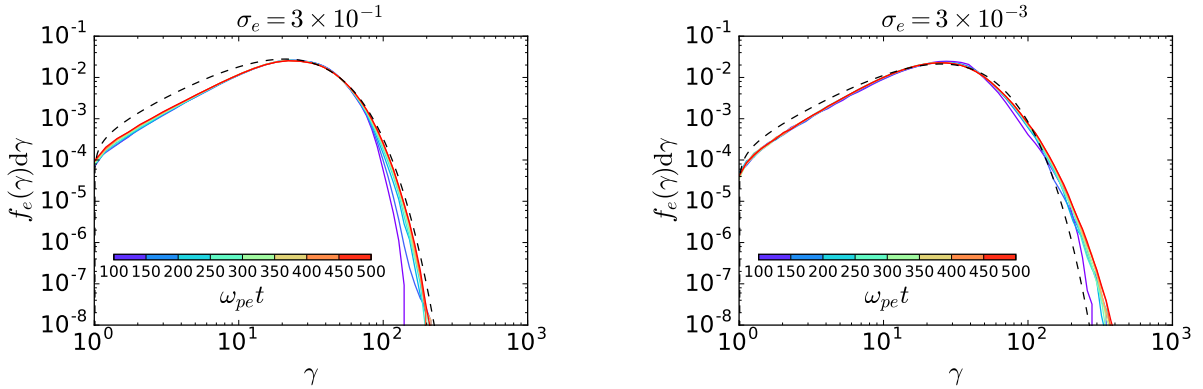


Figure 14. Downstream energy spectra of electrons: $\sigma_e = 3 \times 10^{-1}$ (left) and $\sigma_e = 3 \times 10^{-3}$ (right). The black dashed lines indicate a 3D relativistic Maxwellian fitting result.

In the out-of-plane configuration, however, a suprathermal tail is visible for $\sigma_e = 3 \times 10^{-3}$ (see [Iwamoto et al. 2017](#), Figure 10). This agrees with the simulation result by [Sironi et al. \(2013\)](#). They suggested that the particle acceleration can be explained in terms of a Fermi process due to the strong turbulence generated by the WI and that the suppression of the cross-field diffusion ([Jokipii et al. 1993](#); [Jones et al. 1998](#)) may result in low-level injection of particles into the Fermi process. Our result also confirms that the orientation of the ambient magnetic field affects the efficiency of particle acceleration.

REFERENCES

- Abdo, A. A., Ackermann, M., Ajello, M., et al. 2010, *ApJ*, 715, 429
- Achterberg, A., Wiersma, J., & Norman, C. A. 2007, *A&A*, 475, 19
- Amano, T., & Hoshino, M. 2009, *ApJ*, 690, 244
- Amato, E., & Arons, J. 2006, *ApJ*, 653, 325
- Chang, P., Spitkovsky, A., & Arons, J. 2008, *ApJ*, 674, 378
- Chen, P., Tajima, T., & Takahasi, Y. 2002, *PhRvL*, 89, 161101
- D’Angelo, M., Fedeli, L., Sgattoni, A., Pegoraro, F., & Macchi, A. 2015, *MNRAS*, 451, 3460
- Fried, B. D. 1959, *PhFl*, 2, 337
- Gallant, Y. A., Hoshino, M., Langdon, A. B., Arons, J., & Max, C. E. 1992, *ApJ*, 391, 73
- Gehrels, N., Ramirez-Ruiz, E., & Fox, D. 2009, *ARA&A*, 47, 567
- Hoshino, M. 2008, *ApJ*, 672, 940
- Hoshino, M., & Arons, J. 1991, *PhFIB*, 3, 818
- Hoshino, M., Arons, J., Gallant, Y. A., & Langdon, A. B. 1992, *ApJ*, 390, 454
- Huntington, C. M., Fiuza, F., Ross, J. S., et al. 2015, *NatPh*, 11, 173
- Huntington, C. M., Manuel, M. J., Ross, J. S., et al. 2017, *PhPl*, 24, 041410
- Ikeya, N., & Matsumoto, Y. 2015, *PASJ*, 67, 64
- Iwamoto, M., Amano, T., Hoshino, M., & Matsumoto, Y. 2017, *ApJ*, 840, 52
- Jokipii, J. R., Kóta, J., & Giacalone, J. 1993, *GeoRL*, 20, 1759
- Jones, F. C., Jokipii, J. R., & Baring, M. G. 1998, *ApJ*, 509, 238
- Kaneko, Y., Preece, R. D., Briggs, M. S., et al. 2006, *ApJS*, 166, 298
- Kato, T. N. 2007, *ApJ*, 668, 974

- Kruer, W. L. 1988, *The Physics of Laser Plasma Interactions* (Addison-Wesley)
- Kumar, R., Eichler, D., & Gedalin, M. 2015, *ApJ*, 806, 165
- Kuramitsu, Y., Sakawa, Y., Kato, T., Takabe, H., & Hoshino, M. 2008, *ApJ*, 682, 113
- Langdon, A. B., Arons, J., & Max, C. E. 1988, *PhRvL*, 61, 779
- Lee, L., Kan, J., & Wu, C. 1980, *P&SS*, 28, 703
- Lister, M. L., Aller, M. F., Aller, H. D., et al. 2016, *ApJ*, 152, 12
- Lyubarsky, Y. 2006, *ApJ*, 652, 1297
- Matsukiyo, S., & Scholer, M. 2006, *JGRA*, 111, A06104
- Matsumoto, Y., Amano, T., & Hoshino, M. 2013, *PhRvL*, 111, 215003
- Matsumoto, Y., Amano, T., Kato, T. N., & Hoshino, M. 2015, *Sci*, 347, 974
- Melrose, D. B., Hewitt, R. G., & Dulk, G. A. 1984, *JGRA*, 89, 897
- Melrose, D. B., Rönnmark, K. G., & Hewitt, R. G. 1982, *JGRA*, 87, 5140
- Park, H. S., Huntington, C. M., Fiuza, F., et al. 2015, *PhPl*, 22, 056311
- Schaefer-Rolfs, U., & Tautz, R. C. 2008, *PhPl*, 15, 062105
- Sironi, L., & Spitkovsky, A. 2011, *ApJ*, 726, 75
- Sironi, L., Spitkovsky, A., & Arons, J. 2013, *ApJ*, 771, 54
- Spitkovsky, A. 2005, in *AIP Conf. Proc.*, Vol. 801, *Astrophysical Source of High Energy Particles and Radiation*, ed. T. Bulik, B. Rudak, & G. Madejski (Melville, NY: AIP), 345–350
- Tajima, T., & Dawson, J. 1979, *PhRvL*, 43, 267
- Weibel, Erich, S. 1959, *PhRvL*, 2, 83
- Winske, D., & Quest, K. B. 1988, *JGRA*, 93, 9681
- Wu, C. S., & Lee, L. C. 1979, *ApJ*, 230, 621
- Yang, T.-Y. B., Gallant, Y., Arons, J., & Langdon, A. B. 1993, *ApJ*, 5, 3369
- Yoon, P. H., & Davidson, R. C. 1987, *PhRvA*, 35, 2619